

See discussions, stats, and author profiles for this publication at: <https://www.researchgate.net/publication/258628109>

Stable Hydrogen Storage Cycling in Magnesium Hydride, in the Range of Room Temperature to 300 °C, Achieved Using a New Bimetallic Cr-V Nanoscale Catalyst

ARTICLE *in* THE JOURNAL OF PHYSICAL CHEMISTRY C · DECEMBER 2011

Impact Factor: 4.77 · DOI: 10.1021/jp211254k

CITATIONS

21

READS

14

6 AUTHORS, INCLUDING:



[Beniamin Zahiri](#)

University of Alberta

24 PUBLICATIONS 661 CITATIONS

[SEE PROFILE](#)



[Mohsen Danaie](#)

University of Oxford

34 PUBLICATIONS 477 CITATIONS

[SEE PROFILE](#)



[Babak Shalchi Amirkhiz](#)

Natural Resources Canada

39 PUBLICATIONS 736 CITATIONS

[SEE PROFILE](#)

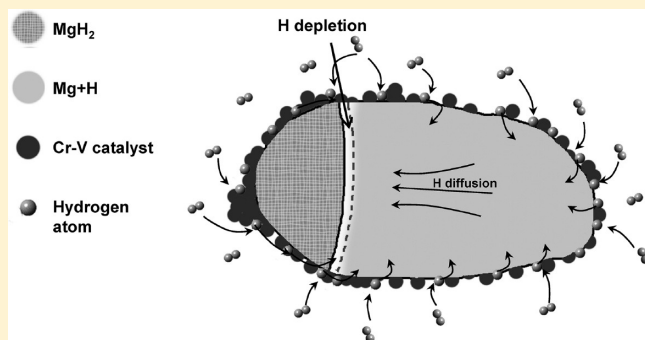
Stable Hydrogen Storage Cycling in Magnesium Hydride, in the Range of Room Temperature to 300 °C, Achieved Using a New Bimetallic Cr-V Nanoscale Catalyst

Benjamin Zahiri,*† Mohsen Danaie,‡ XueHai Tan,† Babak Shalchi Amirkhiz,† Gianluigi A. Botton,‡ and David Mitlin*,†

[†]Chemical and Materials Engineering, University of Alberta and National Research Council Canada, National Institute for Nanotechnology, Edmonton, Alberta, Canada

[‡]Materials Science and Engineering, Brockhouse Institute of Materials Research, McMaster University, Hamilton, Ontario, Canada

ABSTRACT: We created a bimetallic chromium vanadium hydrogen sorption catalyst for magnesium hydride (MgH_2). The catalyst allows for significant room-temperature hydrogen uptake, over 10 cycles, at absorption pressures as low as 2 bar. This is something that has never been previously achieved. The catalyst also allowed for ultrarapid and kinetically stable hydrogenation cycling (over 225 cycles) at 200 and at 300 °C. Transmission electron microscopy analysis of the postcycled samples revealed a nanoscale dispersion of Cr-V nanocrystallites within the Mg or MgH_2 matrix. TEM analysis of the partially absorbed specimens revealed that even at a high absorption pressure, that is, a high driving force, relatively few hydride nuclei are formed at the surface of the pre-existing magnesium, ruling out the presence of any contracting volume (also termed contracting envelope or core shell) type growth. HRTEM of the cycled and desorbed powder sample demonstrated that the bcc Cr-V phase is crystalline and nanoscale. We experimentally demonstrated that the activation energy for hydrogen absorption is not constant but rather evolves with the driving force. This finding sheds new insight regarding the origins of the wide discrepancy in the literature—reported values of the hydrogenation activation energy in magnesium hydride and in related metal hydride systems.



1. INTRODUCTION

Hydrogen storage for fuel-cell based power generation is an active area of research. Because of its high gravimetric capacity of 7.6 wt % and low cost, magnesium hydride (MgH_2) has attracted significant attention as a potential solid-state storage medium. While being less attractive for automotive applications because of its high thermodynamic stability (ΔH^0 MgH₂ formation ≈ -77 kJ/mol), MgH_2 is a candidate for stationary backup power sources where the absorption heat management is a concern and desorption temperatures are less stringent. Magnesium-based alloys, in powder and thin film forms, also attract interest for model studies of hydrogen in metals, optical hydrogen sensing, switchable mirrors, and solar absorber applications, refs 1–13.

To improve the sorption cycling kinetics of magnesium, transition metals are often used as catalyst additions. Researchers have reported significantly accelerated kinetics in binary Mg-V systems relative to other Mg-based alloys.^{14,15} In fact, these Mg-V powder composites displayed some of the fastest hydrogen sorption kinetics of any magnesium-based system. The most commonly reported form of vanadium hydride is $VH_{0.5}$. The reported enthalpy of formation for this hydride ranges from -70 to -83 kJ/mol H₂.^{16,17} Therefore, the formation of $VH_{0.5}$ hydride is expected under temperature/pressure conditions utilized for magnesium.

The formation of hydrides with higher concentrations of hydrogen, for example, $VH_{0.9}$ has also been reported by X-ray measurements.¹⁸ The presence of $VH_{0.81}$ phase in the V-catalyzed magnesium powders has also been reported based on the X-ray analysis.¹⁴ However, as the plateau pressure–composition–temperature (PCT) data showed, the thermodynamics of MgH_2 formation was not altered by the presence of vanadium hydride.

Whereas the sorption behavior and structure of Mg-V system have been widely investigated, Mg-Cr has received much less attention. Similar to other transition metals, Cr is expected to improve the sorption behavior of Mg by lowering the dissociation energy barrier of hydrogen molecules. This has been proven by theoretical calculations on transition-metal-doped Mg surfaces.¹⁹ CrH possesses an enthalpy of formation as low as -6 kJ/mol H²⁰ and is not stable at elevated temperatures under usual testing pressures. The electrochemical sorption behavior of Mg-Cr thin film has also shown an improved kinetics as compared with pure Mg with a reversible capacity of 4.9 wt % for Mg-20Cr.²¹ However, the known relatively slow absorption cycling performance of this binary system along with the theoretical calculations suggests

Received: November 22, 2011

Published: December 12, 2011

that other alloying elements must be added to gain better catalytic performance.^{22,23}

Whereas the kinetic performance of binary Mg-based alloys is clearly improved with respect to pure Mg, even faster sorption rates combined with retained kinetic stability throughout prolonged cycling would be highly desirable. In general, for a material to act as catalyst and maintain its catalytic activity throughout hydrogen sorption cycling the initially nanodispersed catalyst must be stable against coarsening and agglomeration. However, even at temperatures as low as 200 °C, it has been found that the catalyst coarsening accompanied by kinetics degradation occurred over extended sorption cycles.^{22,24} It has been shown that combining two or more transition metals would promote cycling stability presumably due to improved coarsening resistance of the alloy catalyst.^{24–28} Improved catalytic performance would therefore be expected from the Cr-V bimetallic catalyst. A recent neutron reflectometry study performed by our group on 50 nm thick Mg-Cr-V alloy films indeed pointed to markedly improved kinetics and a fundamentally different hydride growth geometric front compared with the baseline Pd-catalyzed Mg films.²⁹ To our knowledge, this is the only existing hydrogen sorption study on this promising ternary system. In the case of the alloy film, at room temperature, the formation of hydride phase occurred uniformly throughout the film rather than at the film–gas interface. Although these results were intriguing, it is not known whether similar behavior would be observed in materials with much larger geometries and hence longer diffusion distances. Furthermore, because of the nature of neutron reflectometry analysis, the microstructural observations were both indirect and nonsite specific in the plane of the film.

This study has two primary goals: We tested a number of ternary Mg-Cr-V compositions, in the form of 1.5 μm thick alloy films, at temperatures ranging from ambient to 300 °C, and observed remarkable kinetics. Therefore, our first goal was to explain the microstructural origin of this performance by employing detailed site-specific transmission electron microscopy (TEM) analysis of the sorbed and partially sorbed microstructures. Our second goal was to correlate these microstructural factors to the calculated activation energies and hence hypothesize about the rate-limiting steps. In the process of doing this through the well-established Johnson–Mehl–Avrami (JMA) analysis, we found that the activation energy for hydrogenation actually varied with the driving force. Although this result is not entirely unexpected, it has been largely overlooked in literature and serves to explain the frustrating lack of correlation in the reported activation energies from various studies.

2. EXPERIMENTAL SECTION

2.1. Synthesis and Analysis Methods. We synthesized the Mg-Cr-V alloys through physical vapor codeposition (magnetron sputtering). The as-synthesized films were 4 inches in diameter with a thickness of 1.5 μm. This minimum dimension was in fact much larger than what is typically used for “bulk” powder studies, where, for example, the particle diameters are in the 200–300 nm range.²⁸ Thin films were magnetron cosputtered (AJA International, ATC ORION S) deposited onto a 4 inch Si (100) substrate that was coated with a hardened (so as not to outgas in the chamber) photoresist at room temperature. We used Ar gas with a purity of grade 5 at a sputtering pressure of 5×10^{-3} mbar, with a maximum base pressure of 5×10^{-8} mbar.

Depositions were done in a sputter-up configuration with continuous substrate rotation. Film thickness and deposition rates were obtained through the use of crystal deposition rate monitor held at the substrate plane. A Pd surface cap was coated onto both sides of the as-synthesized film so as to prevent the oxidation of the magnesium surfaces. A nanoscale layer of Ta was utilized as an intermediate between the Mg-Cr-V and the Pd. This was done because Ta was demonstrated to be effective in reducing the rate of elevated temperature Mg-Pd intermetallic formation during the initial hydrogen absorption step.^{30,31} Inside the sputter system the thin films stack had the following geometry: vacuum/7.5 nm Pd/7.5 nm Ta/1.5 μm Mg-Cr-V/7.5 nm Ta/7.5 nm Pd/photoresist/Si wafer. The deposition rates were the following: Mg 0.3; Pd 0.17; Ta 0.03 nm/sec; and Cr and V varied to adjust for different film stoichiometries. The films had compositions (all in atomic percent) Mg-5Cr-5 V, Mg-7.5Cr-7.5 V, Mg-10Cr-10 V, Mg-7Cr-13 V, Mg-13Cr-7 V, Mg-10 V, and Mg-20 V. Depositions of the catalysts and of the bulk Mg were performed sequentially without any interruption. After deposition, the photoresist was washed away using acetone allowing the films to be fully released from the Si wafer. Release from the substrate allowed the films to be treated as free flakes several tens to about one hundred micrometers in diameter each.

Volumetric absorption and desorption measurements were performed using a Sieverts hydrogen sorption analysis system (Hy-Energy LLC, PCTPro 2000). The cycling measurements were carried out at 25, 200, and 300 °C. Hydrogen was absorbed at a starting pressure of 3 and 4.5 bar during 200 and 300 °C cycling, respectively. For desorption, the samples were put under 15 mbar at 200 °C and 1 bar at 300 °C. The system automatically switched from absorption to desorption, and vice versa, once the sorption rate fell below 0.004 wt %/min. Room-temperature absorption was performed on samples that first underwent 50 absorption/desorption cycles at 200 °C. This “activated” the samples, achieving the steady-state microstructure required for fast kinetics. After the 50th desorption, the sample was cooled to room temperature and absorbed at different pressures in the range of 2–5 bar. After each absorption step, the sample was heated to 200 °C as to be able to desorb under 10–15 mbar.

A partially absorbed sample was prepared for the purpose of microstructural analysis during the absorption reaction. A sample was first cycled 150 times at 200 °C/3 bar. The absorption pressure and temperature were then reduced to 1.5 bar and 185 °C. This temperature–pressure combination resulted in a similar driving force (i.e., deviation from the equilibrium partial pressure plateau). However, the reduced temperature lowered the absorption kinetics sufficiently so as to allow for controlled process interruption. After reaching ~70% (by weight) of the reacted fraction, the sample was quenched to room temperature. For the JMA kinetics analysis and the activation energy measurements, the samples were initially cycled for 50 cycles. The kinetics tests were then performed in the temperature range of 200–240 °C.

Conventional TEM analysis was performed using the JEOL-JEM 2100 microscope, operating at 200 kV accelerating voltage. High-resolution TEM (HRTEM) analysis was performed on an FEI Titan 80-300 microscope equipped with an aberration corrector for the image-forming lens. The accelerating voltage was set at 300 kV, and the spherical aberration coefficient was close to 1 μm during HRTEM experiments. After prolonged hydrogen cycling, the samples still resembled small flakes of thin films combined with aggregated particles. Therefore, additional

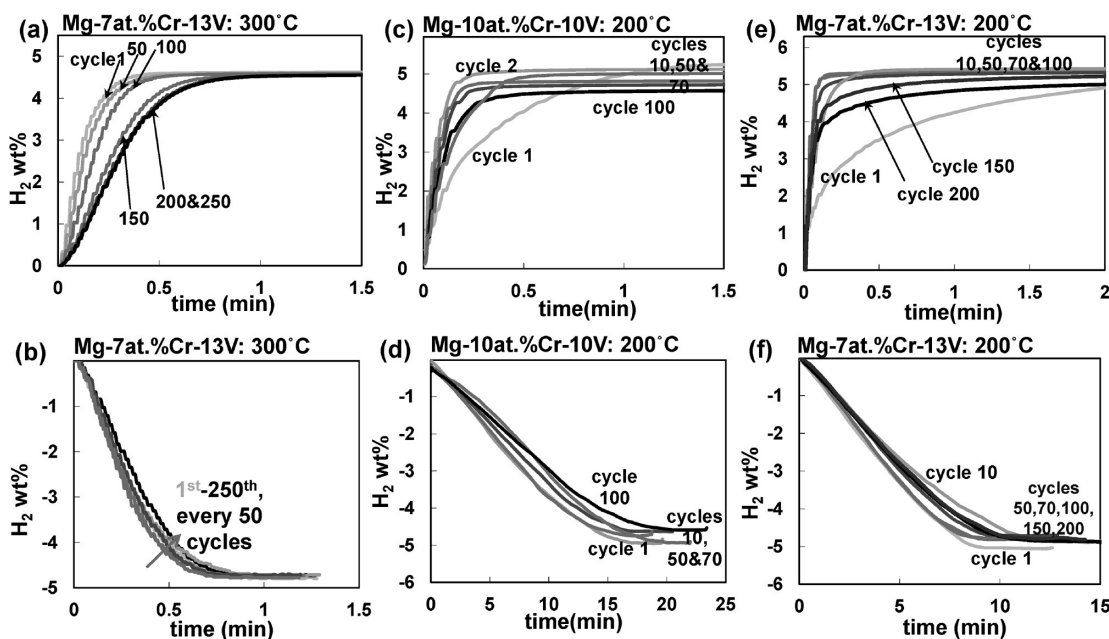


Figure 1. Absorption and desorption hydrogenation cycling data for (a,b) Mg-7 atom %Cr-13 V at 300 °C, (c,d) Mg-7 atom %Cr-13 V at 200 °C, and (e,f) Mg-7 atom %Cr-13 V at 200 °C.

thinning process was required to achieve electron transparency. This was performed via mortar and pestle grinding. The samples then were spread onto a copper grid that was supported by a thin-layer amorphous carbon. TEM analysis of the MgH₂ was performed using a liquid nitrogen-cooled cryostage so as to minimize beam damage and in situ desorption during analysis.³²

X-ray diffraction (XRD) analysis was done using a Rigaku Ultima III X-ray diffractometer with Cu K α radiation source ($\lambda = 1.5406 \text{ \AA}$). To determine the crystallite size of hydride phase, both integral breadth analysis (IBA) and Scherrer methods were utilized.³³ For the IBA, the following formula was used

$$\frac{(\delta 2\theta)^2}{(\tan \theta_0)^2} = \frac{k\lambda}{D} \frac{\delta 2\theta}{\sin \theta_0 \tan \theta_0} + 16e^2 \quad (1)$$

where $\delta 2\theta$ is the integral breadth of the peak in radians and θ_0 is the position of the peak maximum. By plotting the $(\delta 2\theta)^2 / (\tan \theta_0)^2$ versus $(\delta 2\theta) / (\sin \theta_0 \tan \theta_0)$, both values of crystallite size D and microstrain e can be determined. For the Scherrer method, the following equation was used.

$$D = \frac{k\lambda}{\beta \cos \theta_0} \quad (2)$$

where β is the line broadening at half-maximum intensity (fwhm) in radians. In both cases, the values for integral breadth and fwhm were corrected for instrumental effects using a LaB₆ standard obtained from NIST Standard Reference Materials.

2.2. Kinetics Measurements (Theoretical Background). The well-known JMA model can be used to describe magnesium–magnesium hydride phase transformation kinetics.^{34,35} The JMA model assumes the nucleation and growth occurs randomly in the bulk and at the surface. It also assumes that the sample volume is infinite and takes the impingement of growing grains into account. It has been shown that homogeneous and heterogeneous nucleation conditions could be well-described by JMA model.³⁵ This model is also applied to transformations in

which the growth rate is diffusion-limited and interface-controlled. This model is also valid in the cases of nucleation site saturation and constant nucleation rate with constant growth rates. The equation used in JMA model is as follows

$$f = 1 - \exp[-(kt)^n] \quad (3)$$

where k is the rate constant and n is a constant (the so-called Avrami exponent). The Avrami exponent is related to the dimensionality of the growth process and gives information about the rate-limiting step of the reaction. However, such information is not conclusive, especially when n values are small, that is, $n < 1.5$.³⁵ For example, $n = 1$ describes both a diffusion-limited reaction where particles grow along 1-D defects and also an interface-controlled growth with grain boundary nucleation after saturation.³⁵ The Avrami exponent n can be expressed in the general form of $d/m + a$. Here d is the dimensionality of the growth ($d = 1, 2$, and 3) and m indicates interface-controlled ($m = 1$) or diffusion-limited ($m = 2$) growth. The constant a is related to nucleation rate where $a = 0$ for site saturation (constant number of nuclei), $0 < a < 1$ for decreasing nucleation rate, $a = 1$ for constant nucleation rate, and $a > 1$ for increasing nucleation rate.

In general, the rate constant k is a function of temperature and pressure. Therefore, it can be written in the following form.³⁶

$$k = k(P) \cdot k(T) = k(P) \cdot k_0 \exp(-Q/RT) \quad (4)$$

where $k(P)$ is the pressure-dependent term. This term is also referred to as the driving force function. In the pressure-independent term $k(T)$, k_0 is the pre-exponential factor, Q is the overall activation energy, and R is the gas constant. Therefore, to obtain the activation energy of the reaction, one should account for the influence of the pressure during the measurements. The selection of the driving force function is mostly dependent on the rate-limiting step of the reaction. For the metal/hydride transformation, a thermodynamic driving force can be used.³⁶ This function is obtained directly from the

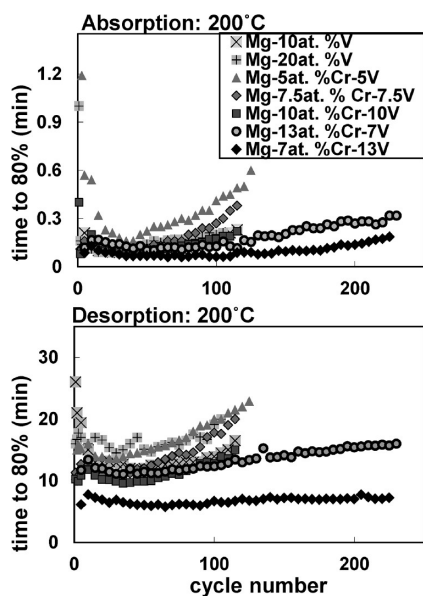


Figure 2. Comparison of the time to sorb 80% of the average maximum hydrogen gravimetric capacity for each composition as a function of sorption cycle number at 200 °C.

chemical potential for a reaction at nonstandard conditions ($\mu = \mu^0 + RT \ln Q$, where Q is the reaction quotient). At a constant temperature, this function has the following form for the case of absorption

$$k(P) = \ln(P/P_{\text{eq}}) \quad (5)$$

where P_{eq} is the equilibrium hydrogen partial pressure for a given temperature.

Rudman showed that in a process where the diffusion is the rate-limiting step, another type of driving force expression could be employed.³⁷ In the derivation, the thermodynamic terms and the diffusivity of the hydrogen atoms were taken into account. The following equation was introduced for the driving force of a diffusion-limited absorption reaction

$$k(P) = 1 - (P_{\text{eq}}/P)^{0.5} \quad (6)$$

In the subsequent kinetic analysis, we will utilize both expressions and demonstrate that they provide similar trends in the activation energy values as a function of pressure.

3. RESULTS

3.1. Hydrogen Sorption. A desorption pressure of 1 bar or higher is required for practical hydrogen storage applications. On the basis of the thermodynamics of Mg/MgH₂ transformation, a temperature of ~300 °C is needed to reach this plateau pressure. In view of this, we examined the cycling performance of Mg-Cr-V ternary system at this temperature. The cycling results of the Mg-7Cr-13 V film at 300 °C are shown in Figure 1a,b. The absorption behavior of this material shows negligible deterioration over 250 cycles, as indicated by Figure 1a. The time to reach 80% of the reaction completion increases from 10 to 25 s. The desorption kinetics (Figure 1b) similarly show minimal degradation, with desorption times being in the range of 25 s over the 250 cycles. Other alloy compositions displayed a similar cycling behavior, with very low levels of kinetics degradation.

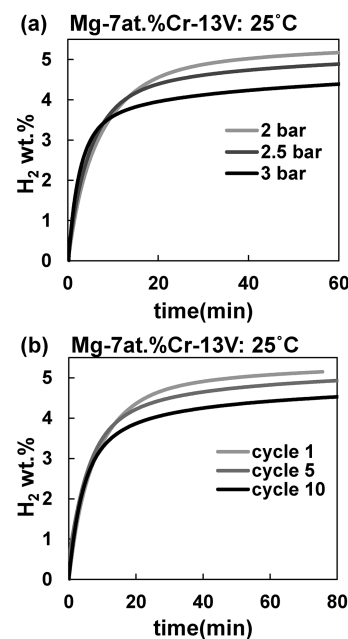


Figure 3. Room-temperature absorption cycling of Mg-7 atom %Cr-13 V alloy desorbed at 200 °C: (a) the effect of charging pressure on the absorption behavior at cycle 1 and (b) cycling performance of the sample at 2 bar absorption pressure.

Figure 1c,d shows the absorption and desorption hydrogenation cycling behavior of the Mg-10Cr-10 V alloy at 200 °C. Figure 1e,f shows the sorption performance of Mg-7Cr-13 V at 200 °C. The graphs show the sorption data for cycles 1, 2, 10, 50, 70, and 100. The system with the V-rich catalyst possesses faster and more stable sorption kinetics. This is highlighted in Figure 2. We are currently investigating the origin of this difference, although it is likely related to the efficacy of V versus that of Cr for dissociating/recombining hydrogen. The Mg-10Cr-10 V alloy was cycled to 115 absorption/desorption cycles before the test was interrupted. Because of its high stability, Mg-7Cr-13 V was cycled to 225 cycles. Even after 225 cycles the hydrogen absorption and desorption kinetics remain remarkably rapid.

A composite plot for the time to absorb and the time to desorb 80% of the mean maximum hydrogen gravimetric capacity at 200 °C is shown in Figure 2. All ternary compositions that were tested are shown, along with the binary Mg-10 V and Mg-20 V alloys. We performed extended cycling on the Mg-13Cr-7 V and Mg-7Cr-13 V systems. Even toward the end of the 225 absorption/desorption cycles, these systems are able to maintain their high sorption rates. The Figure again illustrates that the more V-rich catalyst gives the optimum performance, especially for the hydrogen desorption. Because Mg-7Cr-13 V possessed the most interesting hydrogenation properties, it was chosen for extended microstructural characterization via TEM.

We tested the hydrogen uptake of the ternary alloys at room temperature. Figure 3a shows the room temperature absorption curves of activated Mg-7Cr-13 V sample for three different pressures. Increasing the pressure, although resulting in faster hydrogen uptake initially, leaves the sample with more unreacted Mg. This is inferred from the lower maximum capacity after a certain absorption time. The cycling performance of this composition at room temperature was also tested. Because the material shows a reasonable performance using the pressure of 2 bar,

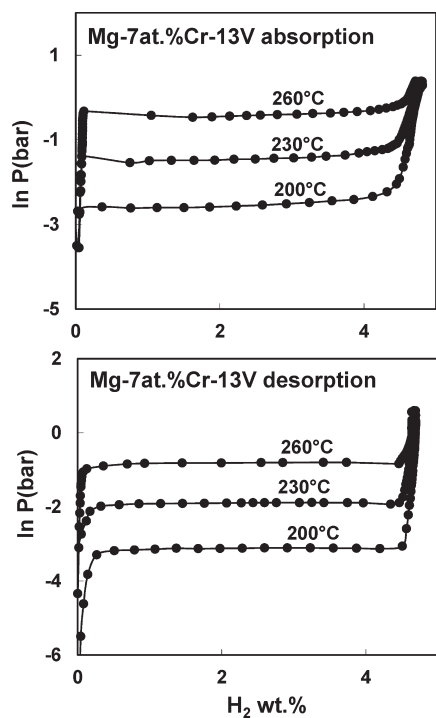


Figure 4. Pressure–composition–temperature (PCT) absorption and desorption results for Mg-7 atom %Cr-13 V.

this pressure was chosen for cycling measurements. For desorption in room temperature, since MgH_2 is thermodynamically stable even at rough vacuum (10–15 mbar), the temperature had to be increased to 200 °C. Figure 3b demonstrates the results for Mg-7Cr-13 V for 10 absorptions/desorptions. Despite experiencing some degradation in the kinetics, the overall performance of the ternary composite at room temperature is remarkable. To our knowledge, there is no report of “bulk” magnesium being absorbed at room temperature many times over at such low pressures. For example, Mg-V binary system has been shown to absorb 2 wt % H_2 in 15 min at room temperature with a hydrogen pressure of 10 bar.¹⁴ In a different study, Mg-Ti H_2 nanocomposite absorbed ~3.5 wt % H_2 within 4 h and under the hydrogen pressure of 40 bar.³⁸

The pressure–composition–temperature (PCT) plots for the Mg-7Cr-13 V system are shown in Figure 4. There is a quantifiable hysteresis between the hydride formation plateau and the hydride decomposition plateau. Such hysteresis is well-known for de/hydrogenation of magnesium alloys and has been attributed to the difference in the irreversible work associated with the nucleation of the hydride in the metal versus the nucleation of the metal in the hydride.²⁰ From the three testing temperatures, on the basis of van't Hoff equation, the enthalpy for hydride formation is −74 kJ/mol H_2 , whereas the enthalpy for hydride decomposition is 80 kJ/mol H_2 . The hydride decomposition enthalpy is on par with what is commonly reported in literature, for example, refs 4, 22, and 27. For van't Hoff equation, several additional temperatures would result in a more accurate enthalpy value. Nevertheless, one can conclusively state that the Cr-V additions do not thermodynamically destabilize MgH_2 , and the reported extremely rapid sorption rates are due to enhanced kinetics. The entropy for hydride formation and decomposition are calculated as −134 and 145 J/K mol H_2 , respectively.

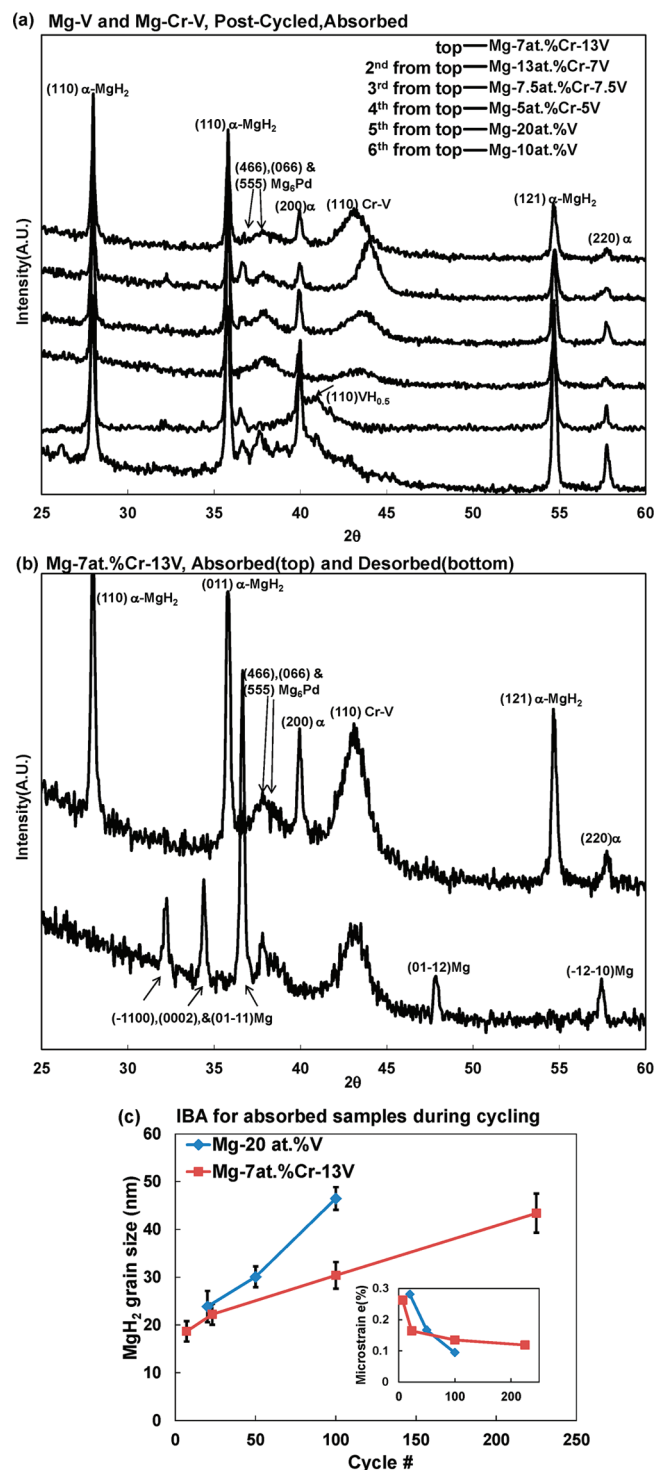


Figure 5. Indexed X-ray diffraction patterns of the (a) postcycled (at 200 °C) binary and ternary samples, all in absorbed state and (b) postcycled Mg-7 atom %Cr-13 V in the absorbed and desorbed states. (c) Integral breadth analysis (IBA) for the cycled binary and ternary alloys.

3.2. Microstructural Analysis. Figure 5a shows the indexed XRD curves for four ternary alloys and Mg-10 and 20 V binary alloys, after they were sorption cycled. The samples are shown in the absorbed state. As is indicated in the data, the primary hydrogen-storing phase is tetragonal $\alpha\text{-MgH}_2$. There is no detectable variation of the $\alpha\text{-MgH}_2$ lattice parameters from the

literature-reported values. Despite the Ta underlayer, the Mg₆Pd intermetallic was still formed. The experimentally overlapping (446), (066), and (555) Mg₆Pd peaks are labeled in the Figure. The detected (224) Mg₆Pd peak present at $2\theta = 21.6^\circ$ is not shown, and the (111) Mg₆Pd at $2\theta = 7.59^\circ$ was outside the range of the detector.

In the absorbed binary Mg-20 V, a vanadium reflection centered at $2\theta = 40.9^\circ$ is detected. Assuming its (110) type reflection gives a lattice parameter of 3.117 Å. From the known lattice parameter for hydrogen-free body-centered cubic (bcc) vanadium ($a = 3.038$ Å), the position of (110) reflection should be at $2\theta = 42.02^\circ$. The lattice expansion indicates the presence of interstitial hydrogen atoms. Using the results from Maeland's work,¹⁸ the composition of such an interstitial hydride is VH_{0.45}.¹⁸ However, on the basis of the suggested V–H phase diagram,¹⁹ such a bcc hydride is stable only at elevated temperatures. At room temperature, where the X-ray measurements were performed, a body-centered tetragonal (bct) interstitial vanadium hydride (VH_x) is expected with $x \approx 0.5$. The bct vanadium hydride has the lattice parameters of $a = 3.302$ and $c = 3.002$ Å. The position of the strongest reflection for this hydride is centered at $2\theta = 40.5^\circ$. The reported values for enthalpy of VH_{0.5} range between -70 and -83 kJ/mol H₂,¹⁶ indicating that they would form both at low temperatures and at 200 °C. Because of the significant peak broadening associated with the reflection in question, it is difficult to identify conclusively the exact structure/stoichiometry of this hydride, and we have therefore left open the possibility that one or both phases may be present.

The XRD patterns of ternary alloys contained characteristic bcc solid solution Cr-V (011) reflection. The next reflection of this bcc structure, that is, (002) is much weaker than (110). The formation of a binary solid solution with bcc structure is expected based on the binary phase diagram. The position of the observed peak depends on the Cr/V atomic ratio, roughly obeying Vegard's law. The lattice parameter of Cr ($a = 2.884$ Å) is smaller than that of V ($a = 3.038$ Å). Hence the Cr-rich composition shows a peak shift toward larger 2θ values, whereas the V-rich composition shows shift towards lower 2θ values. The (110) reflection of all ternary alloys is quite broad, which indicates a nanocrystalline Cr-V phase. The decreasing relative intensity at lower Cr-V contents is due to a decreasing mass fraction of that phase. Figure 5b compares the absorbed and the desorbed Mg-7Cr-13 V. In the desorbed state, α-MgH₂ is replaced by equilibrium magnesium with no variation from the literature reported lattice parameters. Moreover, the position of the (110) reflection of the bcc phase does not change between the absorbed and desorbed states. This indicates that the interstitial hydride does not form during testing, that it forms at elevated temperature but rapidly desorbs during the cool down, or that it forms and remains completely stable during desorption of magnesium. Elevated temperature *in situ* XRD studies would have to be performed to identify conclusively the correct scenario.

Figure 5c shows the IBA results used to determine the MgH₂ grain size during different stages of cycling at 200 °C for a ternary and a binary alloy. For the binary Mg-20 V, MgH₂ grain size starts from 23 nm in the early stages of cycling (cycle 20). This value increases to 30 and 46 nm after 50 and 100 cycles, respectively. As the inset in Figure 5c shows, the microstrain values are in the range of 0.10 to 0.28% for binary samples. For the ternary alloy, an increasing trend in hydride grain size is also observed; however, the rate of increase is relatively smaller than that of the binary alloy. After seven cycles, the MgH₂ grain size is 18 nm.

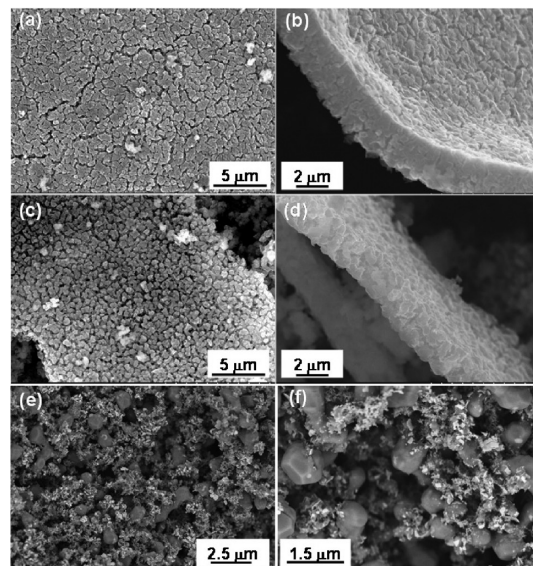


Figure 6. SEM micrographs of Mg-7 atom %Cr-13 V during the course of cycling at 200 °C. (a,b) Top and cross-section views after 50 cycles. (c,d) Material after 120 cycles. (e,f) Material after 225 cycles, highlighting its transformation to an agglomerated powder.

The hydride grain size increases to values of 22 and 30 nm after 23 and 100 cycles, respectively. Eventually after 225 cycles, the hydride grain size for ternary alloy reaches 43 nm, which is similar to that of the binary alloy after 100 cycles. The values for microstrain decrease from 0.24% in the early cycles to 0.11% toward the end of cycling. To determine the crystallite size of Cr-V phase, the Scherrer analysis was performed on the Cr-V (110) reflection, which is the only well-resolved Cr-V peak. In all ternary compositions, the Cr-V crystallite size varies between 5 and 6 nm after extended cycling at 200 °C. During the early stages of cycling, this value is on the order of 3 to 4 nm.

Figure 6 shows the SEM results of Mg-7Cr-13 V samples after 45, 120, and 225 cycles at 200 °C. Figure 6a shows that after 45 cycles the material consists of large flakes with high density of surface cracks. As the cross-section view in Figure 6b depicts, these cracks do not extend all the way through the bulk material. After 120 cycles, the material still resembles a film, although with a much higher density of coarse surface cracks. The plan view image in Figure 6c highlights this progressive film disintegration. As seen in Figure 6d, the cracks propagate deeper into the bulk of the film. The original film is entirely pulverized after 225 cycles. This is highlighted in Figure 6e,f. In this stage, an original film is effectively a powder, consisting of what appears to be a bimodal distribution of agglomerated particles.

Figure 7 shows the results of TEM analysis performed on the Mg-7Cr-13 V sample in its desorbed state after 220 cycles. Figure 7a shows the bright-field (BF) image of the “powder agglomerate”. As this image indicates, the agglomerate consists of a coarse single grain along with numerous ultrafine crystallites. The selected area diffraction (SAD) pattern of this agglomerate is shown in Figure 7b. The spots observed in the SAD pattern are due to the relatively large magnesium grain, which is shown in the dark-field (DF) image in Figure 7c. The DF image is taken near the [1-211]_{Mg} zone axis. Apart from the spot pattern in the SAD pattern, a series of rings is also evident. The simulation of the SAD ring pattern indicates that the observed rings are associated

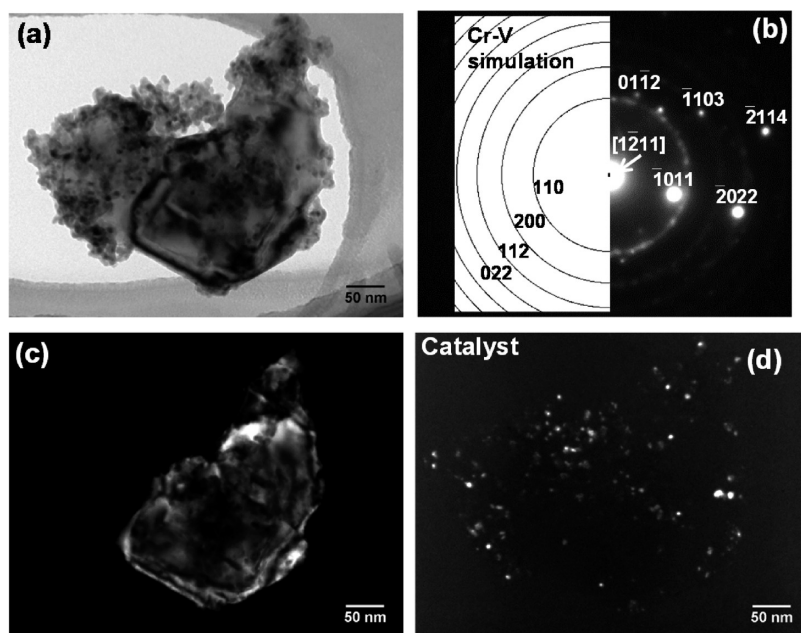


Figure 7. TEM micrographs of desorbed Mg-7 atom %Cr-13 V after 220 cycles at 200 °C. (a) Bright-field micrograph of an agglomerate. (b) Corresponding SAD pattern with the simulated ring pattern of the Cr-V phase and single-crystal Mg. (c) Dark-field micrograph obtained using $g = -1011_{\text{Mg}}$ reflection. (d) Dark-field micrograph, obtained using the portion of $110_{\text{Cr-V}}$ ring, highlighting the Cr-V nanocrystallites.

with the bcc Cr-V phase. Recent TEM studies on the ball-milled MgH_2 powders also showed the presence of MgO on the surface.^{39,40} To rule out the possibility of the MgO as the corresponding phase, the MgO -simulated pattern was also produced (results not shown). The present ring pattern did not match the MgO -simulated pattern at all. Figure 7d shows a DF image of the Cr-V nanocrystallites obtained by using a portion of the $110_{\text{Cr-V}}$ reflection. As this micrograph indicates, the distribution of the catalyst phase is not entirely uniform, although only a fraction of the total Cr-V crystallites shows up in a single DF micrograph. The scale of the nanoparticle distribution is much finer than the dimensions of the Mg crystallite. Both the BF and DF images of the metallic magnesium particle show contrast associated with planar defects such as twins or stacking faults. However there is no evidence of Ashby–Brown-type strain contrast that would be expected if the Cr-V particles were embedded into the bulk of the metallic matrix, for example, refs 41–43. A general hypothesis could therefore be put forward regarding the microstructural evolution in these materials: After codeposition, but before hydrogentation, the catalytic elements have been demonstrated to remain in supersaturated solid solution.²⁹ During the early stages of absorption, a nano-dispersed Cr-V phase forms at the Mg/ MgH_2 grain boundaries. As the sample is progressively cycled, the films crack intergranularly, forming loose agglomerates. As a result, the catalyst nanocrystallites wind up decorating the metal/hydride particle surfaces.

The TEM analysis of a partially absorbed Mg-7Cr-13 V sample, after 150 cycles, is shown in Figure 8. The imaged region contains a metallic magnesium crystallite, a magnesium hydride crystallite, and a large number of catalyst particles. In the observed agglomerate, there may be additional Mg or MgH_2 grains. However, they are not in strong Bragg contrast. Figure 8a shows a BF micrograph of the imaged area. Figure 8b shows an indexed two-beam SAD pattern from the metallic magnesium,

and Figure 8c shows the corresponding DF image. Upon slight tilting of the specimen, we were able to obtain the SAD pattern of the $\alpha\text{-MgH}_2$, also oriented in a strong Bragg orientation with a systematic row of $g = 011\alpha$ reflections excited. The ring pattern from the Cr-V nanocrystallites, which also show up in the SAD, is included in the simulation overlay. The hydride possesses characteristic mottled contrast characteristic of ionic materials and previously reported for MgH_2 .⁴⁴ As Figure 8f indicates, the Cr-V nanocrystallites retain their dense, albeit nonuniform distribution, even after 150 cycles. These images indicate that during absorption the formation and growth of the hydride phase does not take place in the way described by the contracting volume, also known as the contracting envelope or core shell model.⁴⁵ Whereas previously we have demonstrated that during hydrogen desorption there is no evidence of contracting volume in magnesium hydride,⁴⁶ to our knowledge this is the first direct TEM-based observation for the absorption. The driving force for absorption in our experiments was relatively high, whereas the sorption temperature was quite low, as compared with typical MgH_2 studies, for example, refs 14 and 15. Therefore, our results should rule out most possibilities of contracting volume-type phase transformations in magnesium/magnesium hydride, with very large polycrystalline specimens and near-room temperature absorption being the two possible exceptions.

Another feature observed the partially absorbed microstructure is the presence of growth twins. Although deformation twins have been previously reported for high-energy milled MgH_2 powders,^{39,46} growth twins are a new finding. Figure 9 shows an example of such twins, which formed during the fast absorption process. As the SAD pattern in Figure 9b shows, the hydride matrix and twin are close to [131] and [1-31] zone axes, respectively. The twins shown in the DF micrograph (Figure 9c) are imaged using the $g = 211\alpha$ reflection. Without tilting the sample, the MgH_2 matrix could be imaged using the $g = 2-11\alpha$ reflection, as shown in Figure 9d.

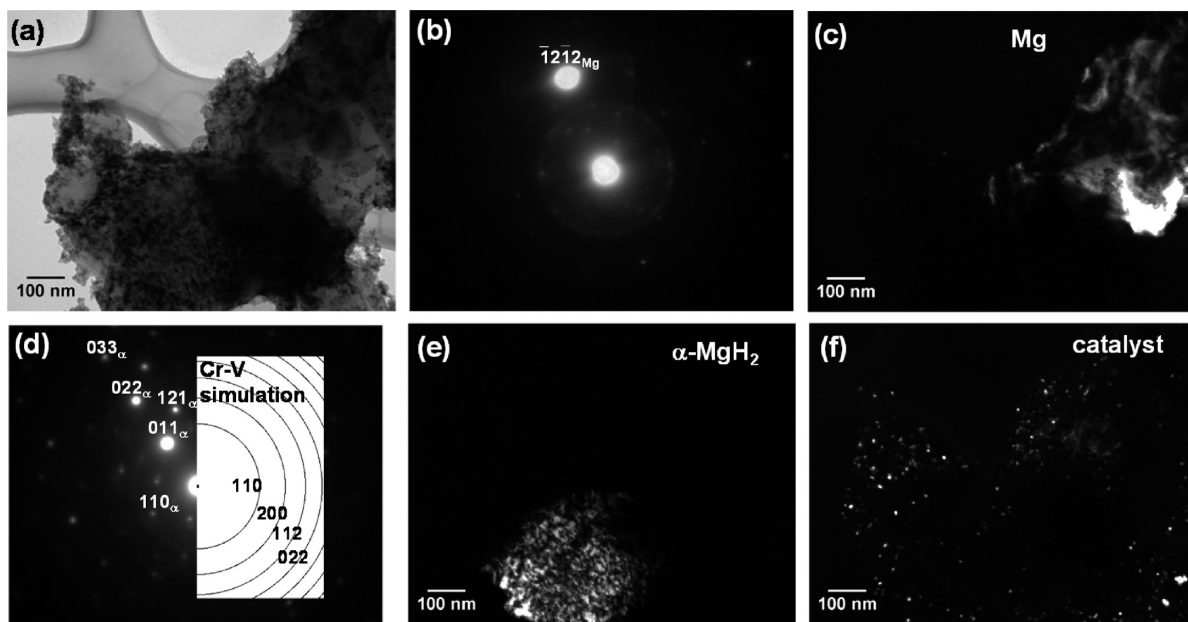


Figure 8. TEM micrographs of Mg-7 atom %Cr-13 V after 150 cycles at 200 °C and partially absorbed. (a) Bright-field micrograph. (b) Corresponding SAD pattern of the metal phase. (c) Dark-field micrograph obtained from $g = -12-12$ reflection. (d) Corresponding SAD pattern of the area near the α -hydride phase. (e) Dark-field micrograph, obtained using the $g = 011_{\text{MgH}_2}$ reflection. (f) Dark-field micrograph obtained using $110_{\text{Cr-V}}$ reflection.

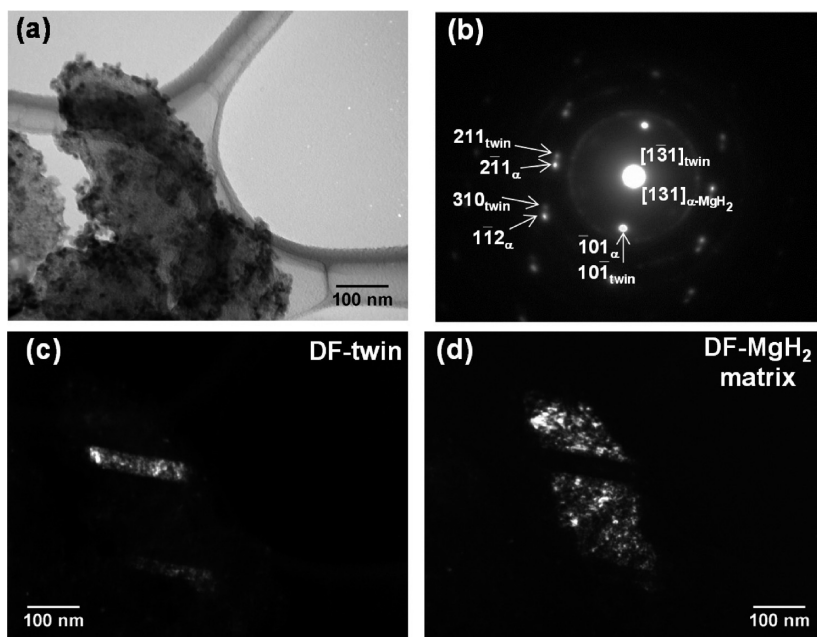


Figure 9. TEM micrographs of partially absorbed Mg-7 atom %Cr-13 V after 150 cycles at 200 °C. (a) Bright-field micrograph. (b) Corresponding SAD pattern. (c) Dark-field micrograph of the twinned MgH_2 obtained using the $g = 211_{\text{twin}}$. (d) Dark-field micrograph obtained from $g = 2-11_{\text{MgH}_2}$ reflection.

For further characterization of the cycled microstructure, we performed high-resolution TEM on the desorbed Mg-7Cr-13 V powder sample that was cycled 270 times. Figure 10a shows the area used for HRTEM in low magnification. The diffraction pattern presented in Figure 10b is from this area, showing the presence of large magnesium single crystals along with a ring pattern of the fine-grained Cr-V bcc phase. The two labeled diffraction spots correspond to the $01-11$ and $01-12$ magnesium

d spacings. Because the angle between these two g vectors is not 49.8° (the corresponding angle in $[01-11]$ zone axis), these spots are from two separate magnesium grains. Micrographs shown in Figure 10c–f are HRTEM data from this region. It can be observed that the secondary bcc phase is crystalline with average grain diameter around 5 to 10 nm. Because of overlapping of these grains, we occasionally encounter Moiré fringes. (Two cases of these fringes are marked with white arrows in

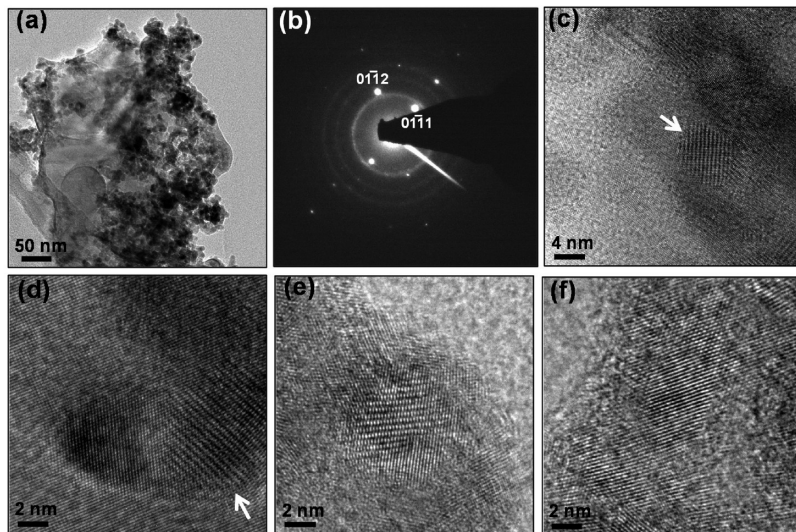


Figure 10. Mg-7 atom %Cr-13 V sample cycled 270 times in desorbed state: (a) low magnification micrograph showing the general area used for HRTEM analysis, (b) diffraction pattern from area in panel a showing large magnesium single crystals and a fine-grained bcc phase, and (c–f) HRTEM micrographs from the area containing the bcc phase.

Figure 10c,d.) This observation is common in microstructures that contain a large density of grain boundaries, for example, nanostructured alloys processed via severe plastic deformation.⁴⁷

3.3. Kinetics Analysis. The value of the activation energy provides an important insight regarding the sorption mechanism. The Avrami exponent, n , is also an important factor in understanding the phase transformation. By fitting the sorption data with the JMA equation, the kinetics parameters k and n are extracted. The two driving force equations (eqs 5 and 6) introduced in the Experimental Section are used for the kinetics analysis. To investigate the influence of applied driving force on the activation energy, we performed absorption tests at eight different driving forces. Every driving force value corresponds to a unique pressure–temperature combination. The pressures vary between the values very close to the equilibrium plateau (~ 0.1 bar at 200°C) to 1.3 bar. The effect of pressure on the absorption kinetics is shown in Figure 11a. The solid lines in the plot represent the fitted curves. As shown in Figure 11b, the Avrami exponent, n , varies between 1.85 at the lowest pressure to 1.45 at the highest pressure.

The rate constants, k , obtained from these fits were used to calculate the activation energies using the standard $\ln(k)$ versus $1/T$ formulation. A weighted least-squares method was used to obtain the activation energy and the corresponding error bars. In this method, a specified weight is defined for each k value. These weights are inversely proportional to the fitting error. The values of activation energies, obtained using the two different driving force equations, are presented in Figure 11c,d. It is worth noting that at a low absorption pressure both equations produce a driving force of a similar magnitude with hence similar activation energies. The thermodynamic driving force shows lower error at lower pressures compared with that of the diffusion-limited reaction. However this trend is reversed at higher pressures. In both cases, activation energies generally decrease with increasing pressure.

Similar to absorption curves a sigmoidal characteristic is also observed in the desorption kinetics. This is illustrated in Figure 11e,f. In contrast with the absorption activation energy measurements, the activation energy for desorption was only tested in a single driving force. At the low desorption pressures

tested, eqs 5 and 6 gave nearly identical values. An activation energy of 91.5 kJ/mol is obtained for the desorption process.

4. DISCUSSION

The variation in the sorption properties for the differing Cr-V compositions is likely related to their interaction with hydrogen, that is, their efficacy for hydrogen dissociation/recombination. The superior sorption performance of Cr-V with an atomic ratio of 1:2 over the 1:1 and 2:1 systems may be rationalized by the catalytic superiority of V over Cr. However, there does exist a unique synergy for the bimetallic system over the elemental catalyst. This warrants further investigation via ab initio modeling methods. In the case of low Cr-V contents, that is, 5–5 and 7.5–7.5, the amount of the catalyst materials seems to be insufficient to achieve the desired kinetic performance.

The TEM observations of the partially absorbed sample revealed some important aspects of the hydrogenation process. Absorption at high pressures and low temperatures did not give rise to the formation of numerous MgH_2 nuclei on the surface of a relatively large particle. Therefore, there is no evidence of a contracting volume structure that would result in such a scenario. (See ref 48 and associated citations for a discussion of this mechanism.) Rather, the formation of isolated MgH_2 nuclei and their subsequent growth into the magnesium crystallites is the hydriding mechanism. Another important feature of partially absorbed microstructure is the presence of twins. It is known that internal stresses occurring during phase transformations promote twinning in nonductile materials. For example, the formation of internally twinned hydride precipitates upon hydrogenation of zirconium has been reported.⁴⁹ The formation of such structure was attributed to the compensation of the internal stress buildup. A similar scenario is envisioned during the hydrogenation of magnesium. During the sorption process, not all grains hydride simultaneously. As a hydride grain formed in the proximity of the untransformed magnesium crystallites, the large volumetric mismatch between the two phases (24.6% with respect to the hydride phase) would create significant stresses around it. This internal

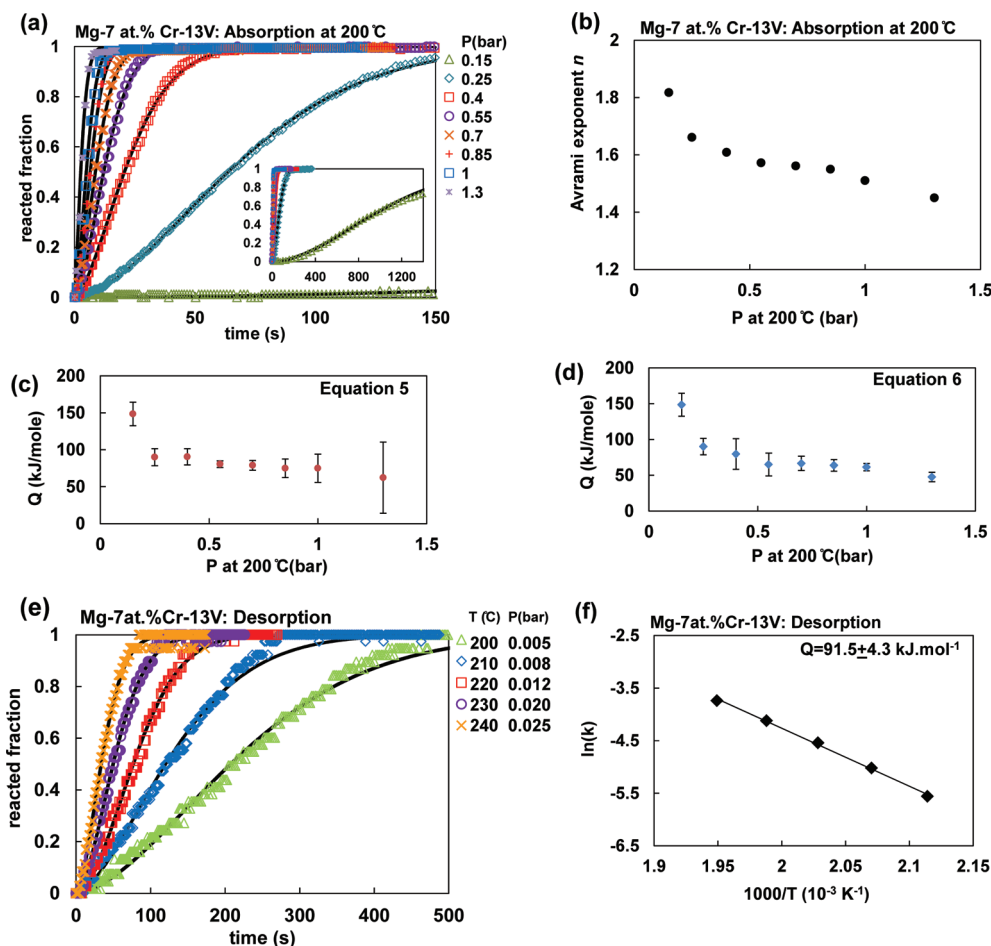


Figure 11. (a) Absorption curves at 200 °C as a function of pressure. The solid lines indicate the fitted curves based on JMA model. (b) Variation of the Avrami exponent, n , as a function of pressure at 200 °C. (c,d) Calculated activation energies based on eqs 5 and 6, respectively. (e) Desorption data at various pressures so as to maintain a constant driving force. (f) Resultant desorption activation energy.

stress, along with a presence of trace levels Cr and V impurities in the hydride, would promote twinning. Because sorption occurs quite rapidly there is insufficient time to anneal the twins out.

The meaning of the activation energy associated with the magnesium to magnesium hydride phase transformation is still debated in literature. Moreover recent modeling work also indicates that because of the interdependence of hydrogen diffusion and dissociation mechanisms a single rate-limiting step may not exist at all.⁵⁰ Our analysis highlights the difficulty of ascribing an exact mechanism to the measured activation energy. The activation energy has contributions from both nucleation and growth steps.³⁵ As demonstrated in Figure 11, the activation energy in fact changes with the driving force almost monotonically. The activation energies are better described by eq 5 at low driving forces. However, as the driving force increases, eq 6 results in more accurate activation energies. The Avrami exponents also showed a decreasing trend with increasing the driving force for absorption. It can be argued that the observed decreasing trend in the Avrami exponent along with the variation of the activation energy with driving force suggests a probable trend in the contribution of nucleation and growth mechanisms to the overall activation energy. Such a trend can be explained by considering the effect of the absorption pressure, that is, the driving force on the rate of the nucleation process. As the

absorption pressure increases, the rate of nucleation also rises toward a situation where at a very high driving force the saturation of nucleation sites occurs in the initial stage of absorption. The decreasing trend in the Avrami exponents corresponds to the variation in the rate of nucleation from decreasing to almost instantaneous. The latter can be expressed using the $d/m + a$ interpretation of the Avrami exponent, where a decreases to zero. Therefore, the drop in the activation energy can be attributed to the diminishing contribution of the activation energy of nucleation. The diffusion-controlled growth with decreasing nucleation rate we suggested here is also described by Christian³⁵ for $1.5 < n < 2.5$.

Perhaps one can argue that at high pressures the measured values of activation energy agree with diffusion of hydrogen in magnesium. For example, on the basis of the work by Renner and Grabke,⁵¹ the activation energy for diffusion of hydrogen in magnesium would be 40 kJ/mol. For the ionic diffusion of hydrogen in the hydride phase a variety of experimental and theoretical studies yielded values ranging from 98 to 166 kJ/mol.^{52–54} Therefore, it seems unlikely that diffusion of hydrogen in the hydride layer could be correlated with the activation energies measured at high pressure.

On the basis of the above-mentioned arguments and the microstructural analysis a general picture of the absorption mechanism can be visualized, as shown in the schematic given

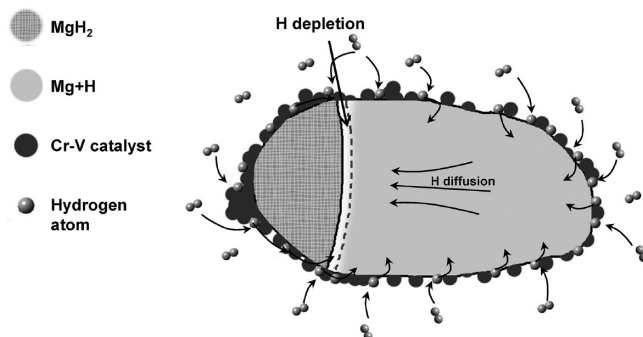


Figure 12. Schematic representation of the proposed hydride growth mechanism.

in Figure 12. Upon the nucleation of the hydride, which is rich in hydrogen atoms, a hydrogen-depleted area is formed around the nucleus. Further growth of hydride is limited by the hydrogen diffusion rate in the Mg matrix. Therefore, it is suggested that the absorption kinetics is governed by nucleation of the new hydride phase along with hydrogen diffusion through the metal matrix. However, we argue that the situation is fairly difficult to resolve based on Avrami analysis, that one should interpret the measured n and Q values with caution, and that it is not surprising that the literature-reported activation energies for nominally identical materials system seldom agree with each other.

5. CONCLUSIONS

A bimetallic chromium vanadium hydrogen sorption catalyst for magnesium hydride (MgH_2) allowed for rapid hydrogen sorption in the temperature range of 25 to 300 °C. The catalyst was sufficiently potent to allow for room-temperature absorption of 5 wt % hydrogen achieved at 2 bar in about 1 h. At 200 and at 300 °C, the Cr-V catalyzed system could be repeatedly sorbed for 225 plus cycles with minimal degradation in the kinetics.

We performed detailed TEM analysis on partially absorbed Mg-7 atom %Cr-13 V sample and HRTEM analysis on the Cr-V catalyst. Analysis demonstrated that the catalyst is both nanoscale and nanodispersed. Early in the absorption cycling, the Cr-V nanocrystallites were most likely situated at the Mg/MgH_2 grain boundaries. With progressive cycling, the films decrepitated into powder agglomerates with the Cr-V particles ended up decorating the Mg/MgH_2 crystallite surfaces. The isolated nucleated hydride grains were much larger than the catalyst particles, and no evidence for a core shell structure was found. HRTEM also confirmed the crystallinity of the Cr-V phase.

Kinetic analysis, performed at 200 °C on the Mg-7 atom %Cr-13 V samples, showed almost a monotonic change in the absorption activation energy with hydrogen pressure. This finding better helps to explain the wide discrepancy in the literature reported values of activation energy. This novel observation, combined with measured Avrami exponents that could correlate to a number of growth scenarios, creates a situation where it is difficult to speculate about the rate-limiting mechanisms for the absorption process.

■ AUTHOR INFORMATION

Corresponding Author

*E-mail: zahirisa@ualberta.ca (B.Z.); dmitlin@ualberta.ca (D.M.).

■ ACKNOWLEDGMENT

This research was supported by NSERC Hydrogen Canada (H2CAN) Strategic Research Network and by NINT NRC. We are grateful to Dr. Peter Kalisvaart for the valuable discussions and comments.

■ REFERENCES

- Srinivasan, S.; Magusin, P. C. M. M.; van Santen, R. A.; Notten, P. H. L.; Schreuders, H.; Dam, B. *J. Phys. Chem. C* **2011**, *115*, 288.
- Yu, X. B.; Guo, Y. H.; Yang, H.; Wu, Z.; Grant, D. M.; Walker, G. S. *J. Phys. Chem. C* **2009**, *113*, 5324.
- Dai, J. H.; Song, Y.; Yang, R. *J. Phys. Chem. C* **2010**, *114*, 11328.
- Kalisvaart, W. P.; Kubis, A.; Danaie, M.; Amirkhiz, B. S.; Mitlin, D. *Acta Mater.* **2011**, *59*, 2083.
- Jeon, K.-J.; Moon, H. R.; Ruminski, A. M.; Jiang, B.; Kisielowski, C.; Bardhan, R.; Urban, J. *J. Nat. Mater.* **2011**, *10*, 286.
- Palmisano, V.; Filippi, M.; Baldi, A.; Slaman, M.; Schreuders, H.; Dam, B. *Int. J. Hydrogen Energy* **2010**, *35*, 12574.
- Tao, S. X.; Notten, P. H. L.; van Santen, R. A.; Jansen, A. P. *J. Phys. Rev. B* **2011**, *83*, 195403.
- Tan, Z. P.; Chiu, C.; Heilweil, E. J.; Bendersky, L. A. *Int. J. Hydrogen Energy* **2011**, *36*, 9702.
- Bendersky, L. A.; Chiu, C.; Skripnyuk, V. M.; Rabkin, E. *Int. J. Hydrogen Energy* **2011**, *36*, 5388.
- Barcelo, S.; Rogers, M.; Grigoropoulos, C. P.; Mao, S. S. *Int. J. Hydrogen Energy* **2010**, *35*, 7232.
- Lang, J.; Huot, J. *J. Alloys Compd.* **2011**, *509*, L18.
- Dura, J. A.; Kelly, S. T.; Kienzle, P. A.; Her, J.-H.; Udovic, T. J.; Majkrzak, C. F.; Chung, C.-J.; Clemens, B. M. *J. Appl. Phys.* **2011**, *109*, 093501.
- Nielsen, T. K.; Besenbacher, F.; Jensen, T. R. *Nanoscale* **2011**, *3*, 2086.
- Liang, G.; Huot, J.; Boily, S.; Van Neste, A.; Schulz, R. *J. Alloys Compd.* **1999**, *291*, 295.
- Liang, G.; Huot, J.; Boily, S.; Schulz, R. *J. Alloys Compd.* **2000**, *305*, 239.
- Schlappbach, L. In *Hydrogen in Intermetallics I*; Schlappbach, L., Ed.; Springer-Verlag: Berlin, 1999.
- Silveira, M. G.; Gremaud, R.; Baldi, A.; Schreuders; Damd, B.; Griessen, R. *Int. J. Hydrogen Energy* **2010**, *35*, 6959.
- Maeland, A. J. *J. Phys. Chem.* **1964**, *68*, 2197.
- Kecik, D.; Aydinol, M. K. *Surf. Sci.* **2009**, *603*, 304.
- Griessen, R.; Riesterer, T.; Flanagan, T. B.; Oates, W. A. In *Hydrogen in Intermetallics I*; Schlappbach, L., Ed.; Springer-Verlag: Berlin, 1988.
- Niessen, R. A. H.; Notten, P. H. L. *Electrochem. Solid-State Lett.* **2005**, *8*, A534.
- Zahiri, B.; Amirkhiz, B. S.; Mitlin, D. *Appl. Phys. Lett.* **2010**, *97*, 083106.
- Tao, S. X.; Notten, P. H. L.; van Santen, R. A.; Jansen, A. P. *J. Phys. Rev. B* **2010**, *82*, 125448.
- Zahiri, B.; Amirkhiz, B. S.; Danaie, M.; Mitlin, D. *Appl. Phys. Lett.* **2010**, *96*, 013108.
- Kalisvaart, W. P.; Harrower, C. T.; Haagsma, J.; Zahiri, B.; Luber, E. J.; Ophus, C.; Poirier, E.; Fritzsche, H.; Mitlin, D. *Int. J. Hydrogen Energy* **2010**, *35*, 2091.
- Kale, A.; Bazzanella, N.; Checchetto, R.; Miotello, A. *Appl. Phys. Lett.* **2009**, *94*, 204103.
- Zahiri, B.; Harrower, C. T.; Amirkhiz, B. S.; Mitlin, D. *Appl. Phys. Lett.* **2009**, *95*, 103114.
- Amirkhiz, B. S.; Zahiri, B.; Kalisvaart, W. P.; Mitlin, D. *Int. J. Hydrogen Energy* **2011**, *36*, 6711.
- Kalisvaart, W. P.; Luber, E.; Fritzsche, H.; Mitlin, D. *Chem. Commun.* **2011**, *47*, 4294.
- Fritzsche, H.; Ophus, C.; Harrower, C. T.; Luber, E.; Mitlin, D. *Appl. Phys. Lett.* **2009**, *94*, 241901.

- (31) Fritzsche, H.; Saoudi, M.; Haagsma, J.; Ophus, C.; Luber, E.; Harrower, C. T.; Mitlin, D. *Appl. Phys. Lett.* **2008**, *92*, 121917.
- (32) Danaie, M.; Mitlin, D. *J. Alloys Compd.* **2009**, *476*, 590.
- (33) Klug, H. P.; Alexander, L. E. *X-ray Diffraction Procedures*; John Wiley and Sons: New York, 1974; p 643.
- (34) Avrami, M. *J. Chem. Phys.* **1940**, *8*, 212.
- (35) Christian, W. *The Theory of Transformations in Metals and Alloys*; Pergamon: Oxford, U.K., 1975.
- (36) Forde, T.; Maehlen, J. P.; Yartys, V. A.; Lototsky, M. V.; Uchidab, H. *Int. J. Hydrogen Energy* **2007**, *32*, 1041.
- (37) Rudman, P. S. *J. Appl. Phys.* **1979**, *50*, 7195.
- (38) Lu, J.; Choi, Y.; Fang, Z. Z.; Sohn, H. Y.; Rönnebro, E. *J. Am. Chem. Soc.* **2010**, *132*, 6616.
- (39) Amirkhiz, B. S.; Danaie, M.; Mitlin, D. *Nanotechnology* **2009**, *20*, 204016.
- (40) Beattie, S. D.; Setthanan, U.; McGrady, G. S. *Int. J. Hydrogen Energy* **2011**, *36*, 6014.
- (41) Mitlin, D.; Radmilovic, V.; Dahmen, U.; Morris, J. W. *Metall. Mater. Trans. A* **2001**, *32A*, 197.
- (42) Mitlin, D.; Radmilovic, V.; Morris, J. W. *Metall. Mater. Trans. A* **2000**, *31A*, 2697.
- (43) Mitlin, D.; Radmilovic, V.; Morris, J. W. *Mater. Sci. Eng., A* **2001**, *301*, 231.
- (44) Amirkhiz, B. S.; Danaie, M.; Barnes, M.; Simard, B.; Mitlin, D. *J. Phys. Chem. C* **2010**, *114*, 3265.
- (45) Rudman, P. S. *J. Less-Common Met.* **1983**, *89*, 93.
- (46) Danaie, M.; Tao, S. X.; Kalisvaart, W. P.; Mitlin, D. *Acta Mater.* **2010**, *58*, 3162.
- (47) Rentenberger, C.; Waitz, T.; Kärnthal, H. P. *Scr. Mater.* **2004**, *51*, 789.
- (48) Bloch, J.; Mintz, M. H. *J. Alloys Compd.* **1997**, *253*, 529.
- (49) Bradbrook, J. S.; Lorimer, G. W.; Ridley, N. J. *Nucl. Mater.* **1972**, *42*, 142.
- (50) Borgschulte, A.; Gremaud, R.; Griessen, R. *Phys. Rev. B* **2008**, *78*, 094106.
- (51) Renner, J.; Grabke, H. J. *Z. Metallkd.* **1978**, *67*, 639.
- (52) Conradi, M. S.; Mendenhall, M. P.; Ivancic, T. M.; Carl, E. A.; Browning, C. D.; Notten, P. H. L.; Kalisvaart, W. P.; Magusin, P. C. M. M.; Bowman, R. C., Jr.; Hwang, S.-J.; Adolphi, N. L. *J. Alloys Compd.* **2007**, *446*, 499–503.
- (53) Hao, S.; Sholl, D. *Appl. Phys. Lett.* **2008**, *93*, 251901.
- (54) Cermak, J.; Kral, L. *Acta Mater.* **2008**, *56*, 2677.

■ NOTE ADDED AFTER ASAP PUBLICATION

This article was published ASAP on January 11, 2012 without the author's corrections. The correct version was published on January 19, 2012.